Electronic Supplementary Material (ESI) for Nanoscale.

Supporting Information

Plasmonic Sensor with High Figure of Merit Based on Differential Polarization Spectra of Elliptical Nanohole Array

Bin Ai,* Pradip Basnet, Steven Larson, Whitney Ingram, and Yiping Zhao

Department of Physics and Astronomy, University of Georgia, Athens, GA 30602, USA

Section SI. Evidence to Normalize the Transmission Spectra.

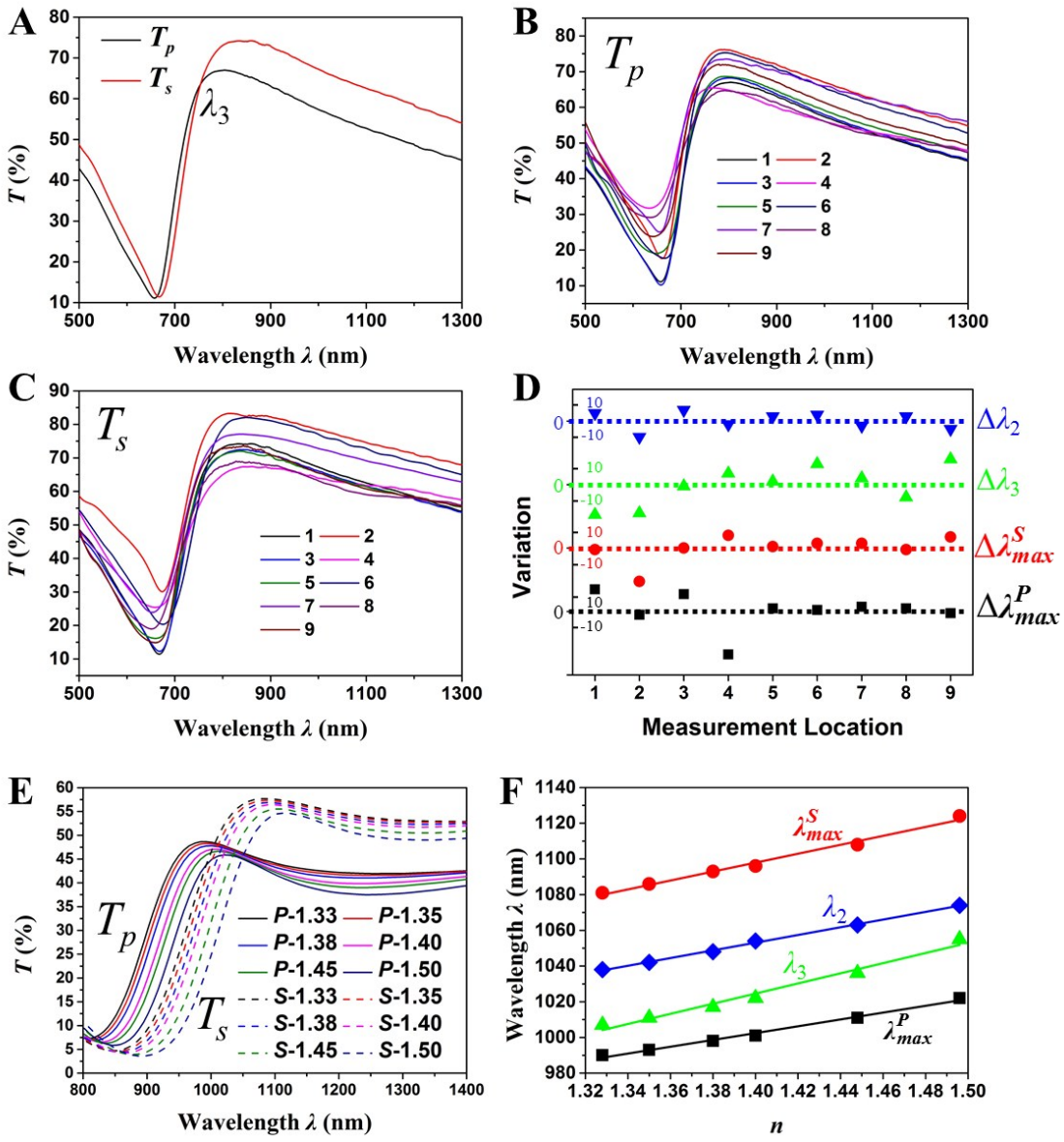

Figure S1. (A) Original T_p and T_s of the Ni based elevated elliptical nanohole array deposited at 40° (Sample EE$^{40°}$). The cross-point wavelength from the original spectra is defined as λ_3. Original experimental (B) T_p and (C) T_s of the Ni based Sample EE$^{40°}$ measured at different locations. (D) Variations of the λ^P_{max}, λ^S_{max}, λ_3 and λ_2 for repeated measurements in (B and C), whose standard deviations are 11 nm, 8 nm, 13 nm, and 5 nm, respectively. (E) Unnormalized T_p and T_s of the ENA in different n calculated by FDTD. (F) Linear fits of the

changes of λ_{max}^{P} (R^2 = 0.98950), λ_{max}^{S} (R^2 = 0.98666), λ_2 (R^2 = 0.99732), and λ_3 (R^2 = 0.97387) as a function of n.

The zero-crossing points (ZCPs, λ_2) from the normalized T_p and T_s are used due to their better linear dependence on the changing refractive index (n) as well as better stability/reliability in experimental measurements. Such a strategy has been validated by both experimental results and FDTD calculations, as shown in Figure S1.

The ZCP from the original T_p and T_s is defined as λ_3 as shown in Figure S1A. Figures S1B and S1C show the nine repeated measurements of T_p and T_s for the Ni based Sample EE$^{40°}$ at different sample locations. The variations of the λ_{max}^{P}, λ_{max}^{S}, λ_3, and λ_2 around their average values are shown in Figure S1D, whose standard deviations are 11 nm, 8 nm, 13 nm, and 5 nm, respectively. Obviously, λ_2 has the smallest variation, showing the best accuracy in experimental measurements, while λ_3 varies the most in the repeated measurements. Experimentally, the spectra will be affected by many factors, such as the uniformity of the sample, the defect in the sample, and the measurement conditions. The ZCPs will not only be determined by the peak and dip locations, but also their relative transmission. The large variations in λ_3 shows that those experimental conditions have a significant effect, while the normalized spectra can significantly reduce these effects.

In addition, for an ideal structure, λ_3 and λ_2 follow the same trend as a function of n, which has been demonstrated by FDTD calculations, as shown in Figures S1E and S1F. Figure S1E shows the original T_p and T_s spectra in Figure 1 for different n calculated by FDTD. It can be seen that overall the T_p shifts to blue and has smaller transmission as compared with T_s. The

changes of λ_2, λ_3 as well as λ_{max}^{P}, λ_{max}^{S} as a function of n are plotted in Figure S1F, and they all follow a linear relationship with very similar trends. The calculated slopes of the λ_{max}^{P}, λ_{max}^{S}, λ_2, and λ_3 are 191, 250, 284 and 216 nm RIU^{-1}, respectively. Thus, theoretically, both λ_2 and λ_3 can use in sensing.

Section SII. Characterization of ENAs

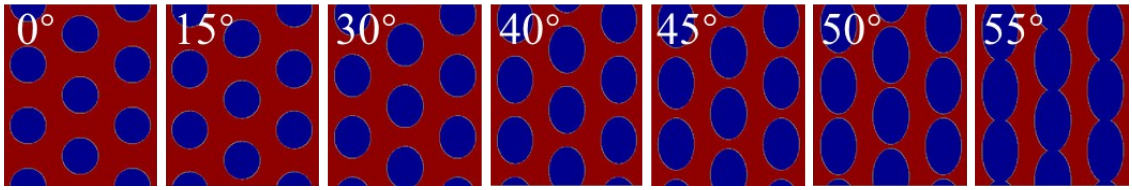

Figure S2. ENA morphologies at θ = 0°, 15°, 30°, 40°, 45°, 50°, and 55°, respectively, where the deposited Ag films red and the underlying substrate blue, calculated by a home-made MatLab code.[1] The aspect ratio become larger with increasing θ. When θ = 55°, zigzag Ag stripes will be formed on the substrates, rather than elliptical holes.

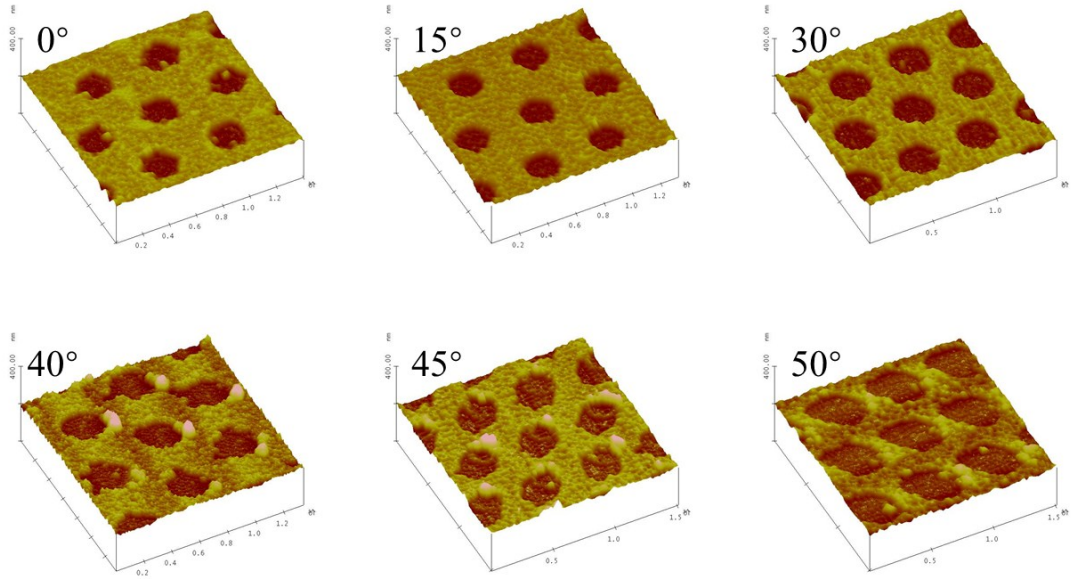

Figure S3. 3D AFM images of the ENAs fabricated at θ = 0°, 15°, 30°, 40°, 45° and 50°, respectively. As the θ increases, the edge and surface roughness also increases.

Section SIII. Sensing Performances of ENAs

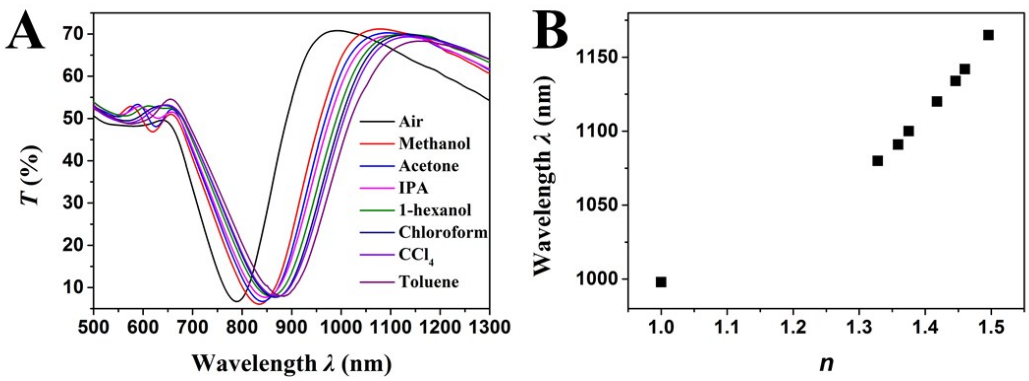

Figure S4. (A) Transmission spectra of the Sample $E^{0°}$ in different surrounding environments. (B) Plot of the wavelength of the main transmission peak as a function of *n*.

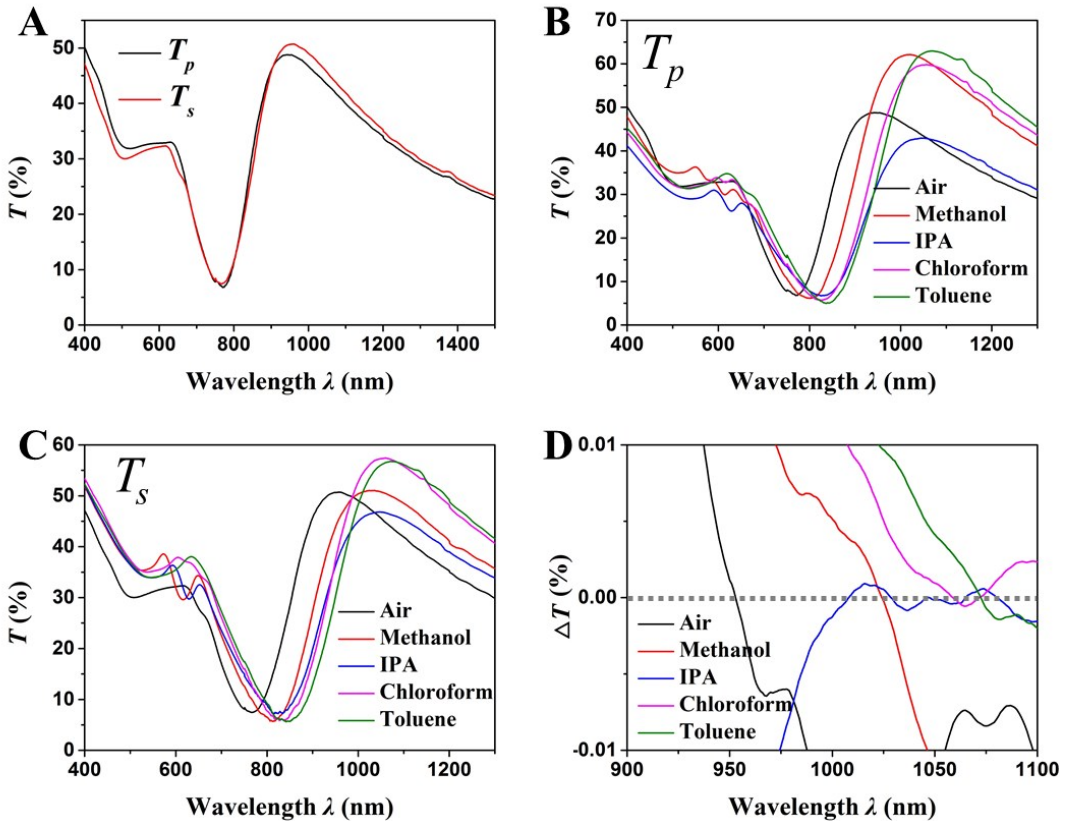

Figure S5. (A) T_p and T_s of the Sample $E^{15°}$ in air. (B) T_p and (C) T_s of the Sample $E^{15°}$ in different surrounding environments. (D) Spectra ΔT of the Sample $E^{15°}$ in different surrounding environments. The grey dotted line indicates $\Delta T = 0$.

As shown in Figure S5A, the difference of T_p and T_s is very small for the Sample $E^{15°}$. Although λ_{max}^{P} and λ_{max}^{S} show red-shifts with increasing n (Figures S5B and S5C), λ_2 shifts unpredictably (Figure S5D). The small difference of T_p and T_s tends to generate more than one ZCP, as shown in Figure S5D, which means λ_2 of the Sample $E^{15°}$ cannot be obtained consistently.

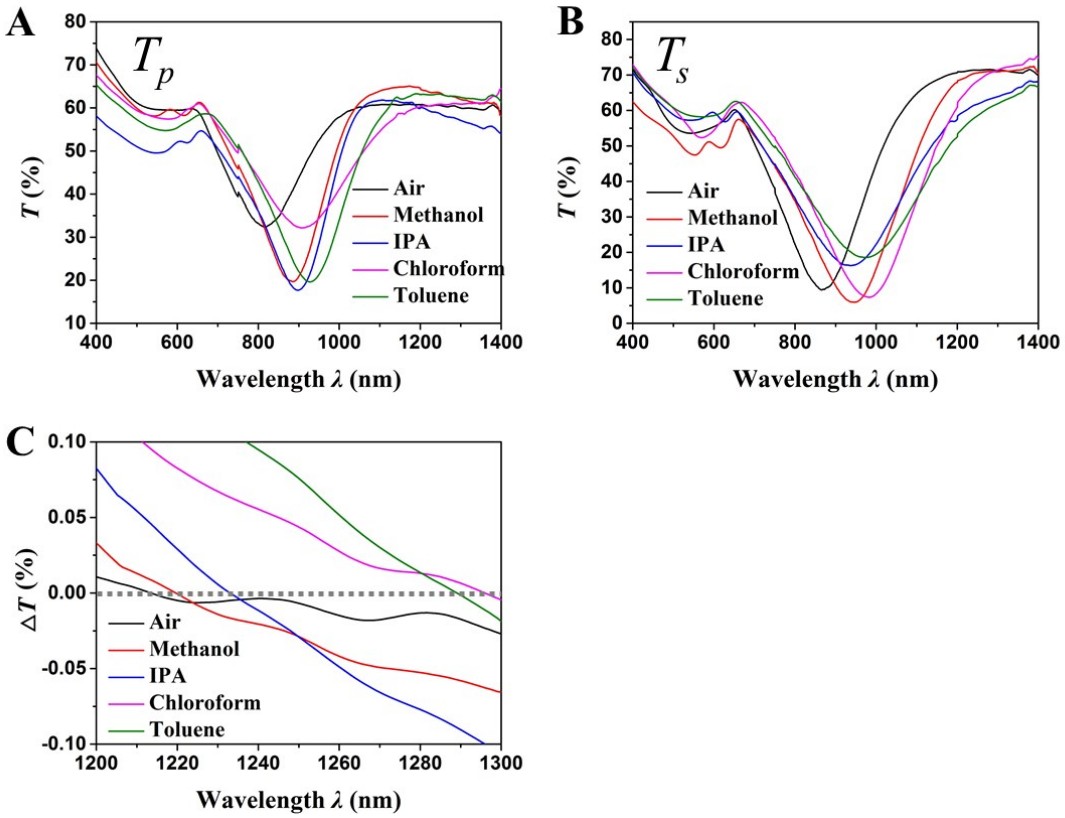

Figure S6. (A) T_p and (B) T_s of the Sample $E^{40°}$ in different surrounding environments. (C) Spectra ΔT of the Sample $E^{40°}$ in different surrounding environments. The grey dotted line indicates $\Delta T = 0$.

Figures S6A and S6B show T_p and T_s of the Sample $E^{40°}$ in different surrounding environments, respectively. Qualitatively, they both show red-shifts with increasing n. However, the broad peaks not only cause trouble for normalization, but also makes it difficult to identify λ_2. The resulted λ_2 shown in Figure S6C does not shift consistently with n.

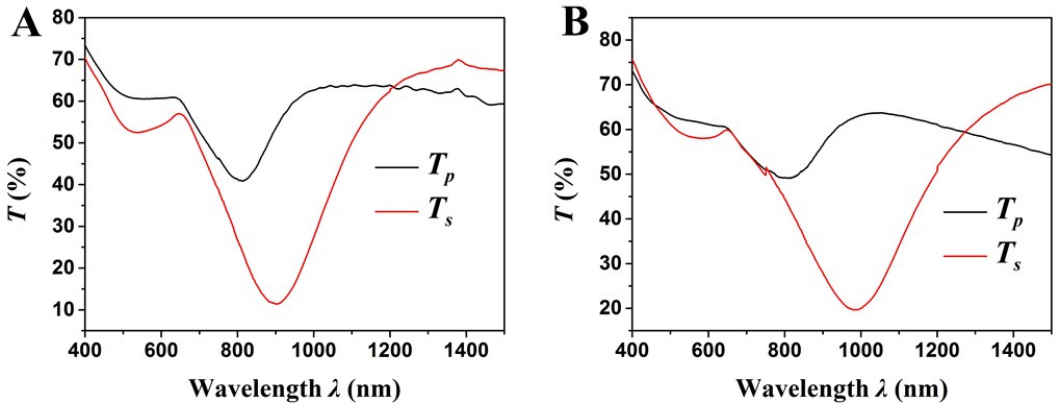

Figure S7. T_p and T_s of the Samples (A) $E^{45°}$ and (B) $E^{50°}$ in air.

As shown in Figure S7, the peaks of the Samples $E^{45°}$ and $E^{50°}$ are broader than those of the Sample $E^{40°}$. Due to the same reason discussed in Figure S6, they also cannot be used with this method.

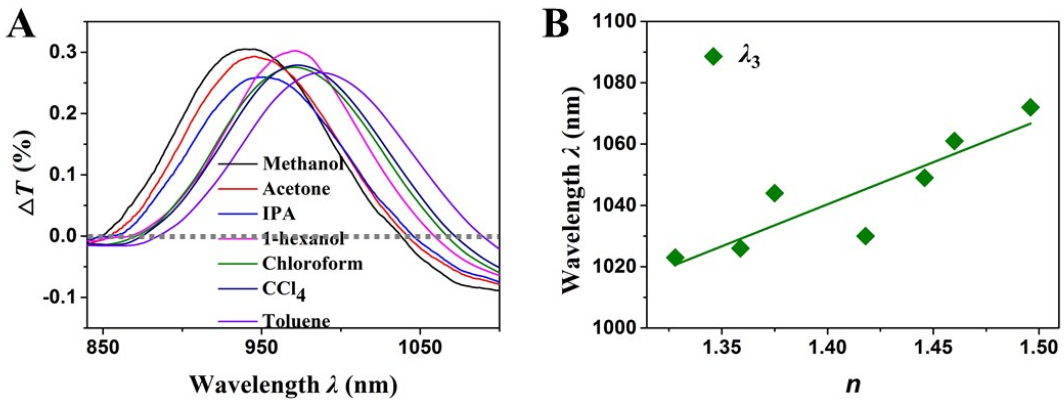

Figure S8. (A) Spectra ΔT of the Sample $E^{30°}$ in different liquids. (B) Linear fit of the peak shift of λ_3 as a function of n. The fitting linearity of λ_3 ($R^2 = 0.75476$) is much worse than that of λ_2 ($R^2 = 0.96296$). This is consistent with the discussion in Section SI.

Section SIV. Influence of Instrument Noise

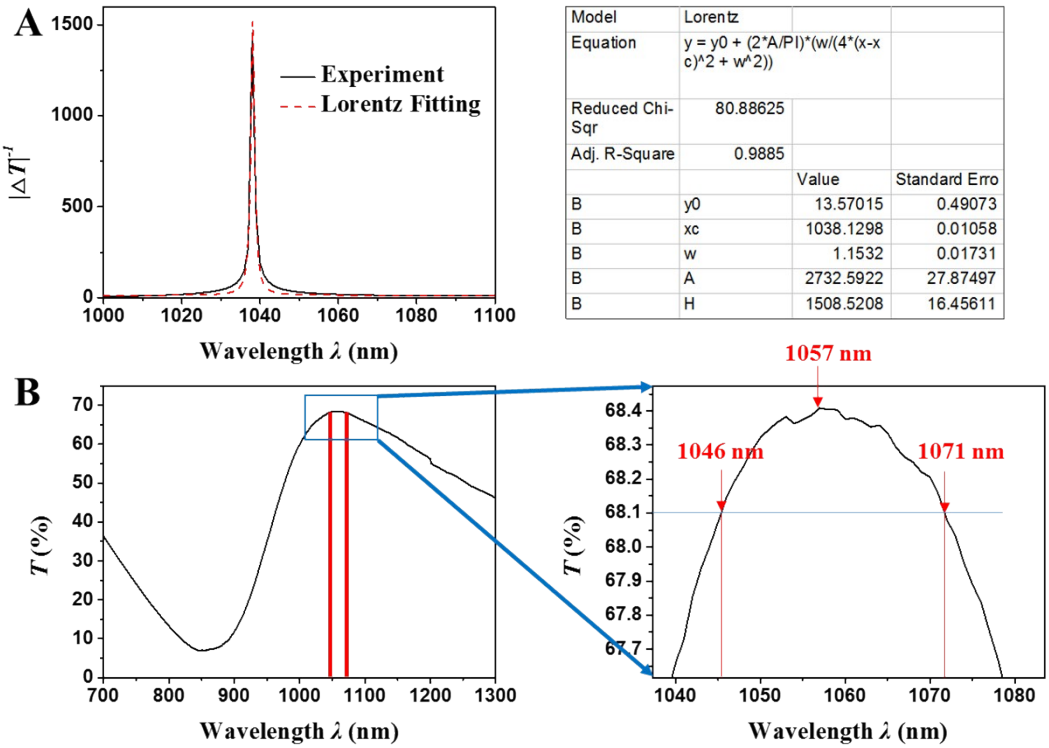

Model	Lorentz		
Equation	y = y0 + (2*A/PI)*(w/(4*(x-xc)^2 + w^2))		
Reduced Chi-Sqr	80.88625		
Adj. R-Square	0.9885		
		Value	Standard Erro
B	y0	13.57015	0.49073
B	xc	1038.1298	0.01058
B	w	1.1532	0.01731
B	A	2732.5922	27.87497
B	H	1508.5208	16.45611

Figure S9. (A) Experimental $|\Delta T|^{-1}$ and the Lorentz fitting of λ_2 of the Sample $E^{30°}$ in methanol. The factor xc is the peak wavelength, whose standard error is 0.01058. (B) T_P of the Sample $E^{30°}$ in methanol. The red lines indicate the error range. The area in the blue rectangle is shown in the right figure. The peak wavelength is 1059 ± 12 nm.

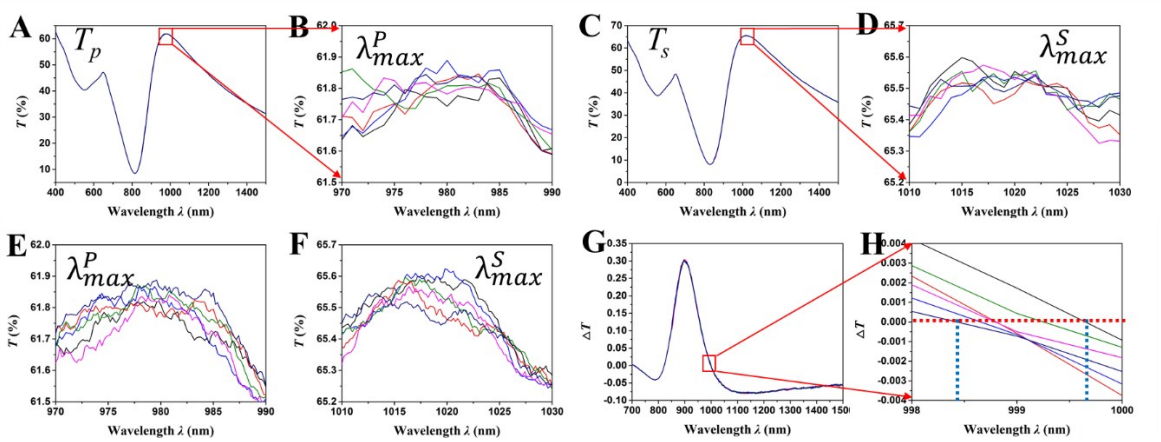

Figure S10. (A) Spectra T_p of the Sample E$^{30°}$ measured at the same position. (B) Amplification of the area indicated by the red rectangle in (A). (C) Spectra T_s of the Sample E$^{30°}$ measured at the same position. (D) Amplification of the area indicated by the red rectangle in (C). The spectra in (A-D) were measured with 1-nm instrument resolution. Spectra (E) T_p and (F) T_s measured at the same position with 0.2-nm data pitch. The spectra are amplified at the peak λ^P_{max} and λ^S_{max}. (G) Spectra ΔT of the Sample E$^{30°}$ achieved from T_p and T_s measured with 1-nm instrument resolution. (H) Amplification of the area indicated by the red rectangle in (G). The dotted lines indicate the ZCPs.

As shown in Figure S10A-D, the spectra were measured repeatedly for six times at the same location of the same sample. The instrument resolution for the measurements in Figure S10A-D is 1 nm. There is a deviation of about ± 4 nm for the peak wavelength λ^P_{max} and λ^S_{max} due to the instrument noise. It should keep in mind that the deviation is achieved by limited measuring times (six times). The values of the error calculated in Figure S9 are based on the manual of the instrument. When the spectra were measured using the resolution of 0.2 nm in Figures S10E and S10F, the deviation is also at about ±4 nm (Figures S10E and S10F). This demonstrates that 1-nm resolution would not lead to higher influence of instrument noise. For

spectra ΔT in Figures S10G and S10H, the deviation of the ZCP is ± 0.7 nm. It is found that using differential spectra is easy to determine ZCPs and can lower the influence of instrument noise in determining the peak positions. However, using the peak fitting method for a broad peak, it is hard to determine the peak location with intensity fluctuation. This is due to the fact that the slope of the difference spectrum at the ZCP is large, so the noise can hardly affect the ZCP determination; while for the peak fitting, the slope near the peak location is nearly zero, so small intensity variation by the noise could significantly vary the determination of peak position.

Section SV. Local *E*-fields of ENAs Calculated by FDTD

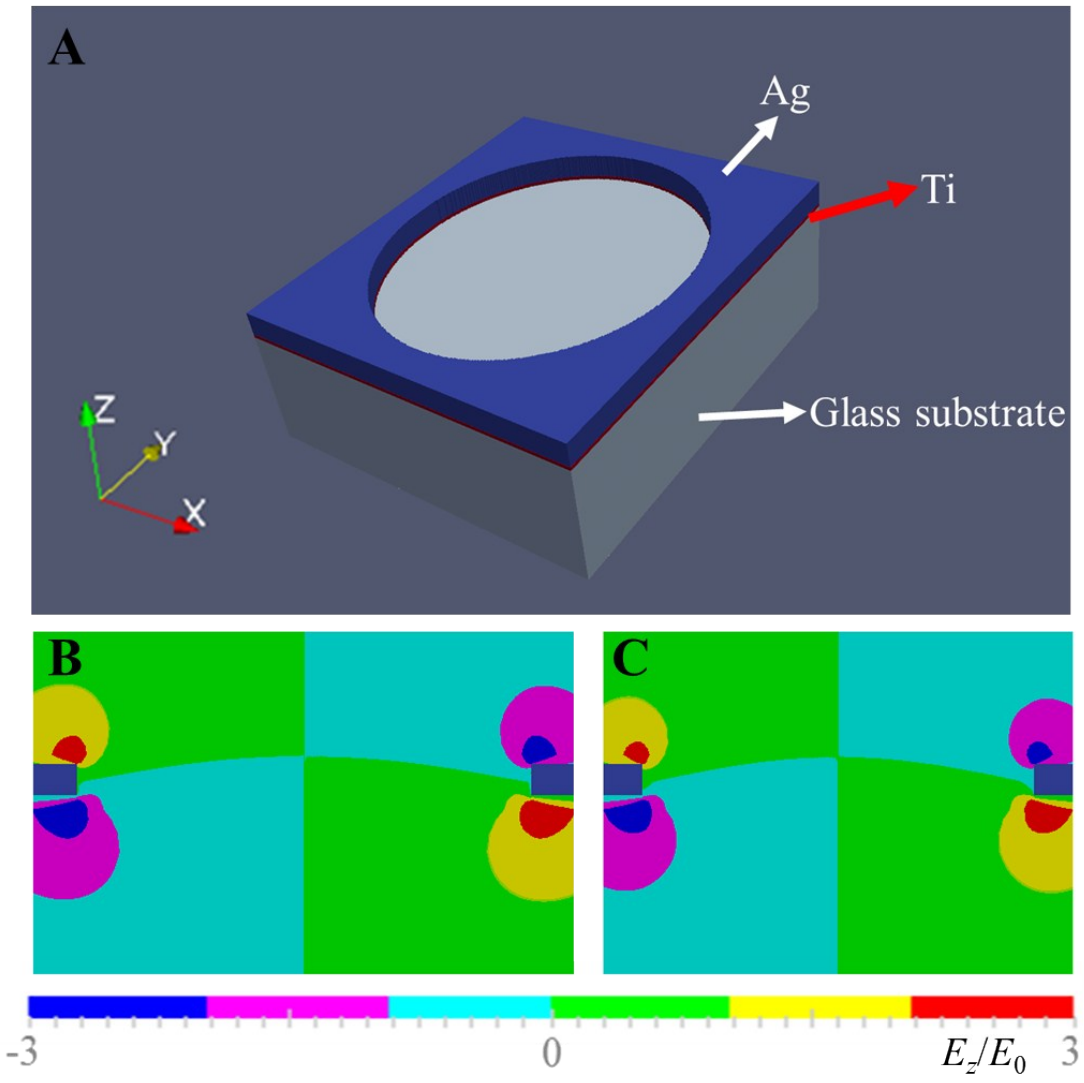

Figure S11. (A) The structure model of the Sample $E^{30°}$ used in the FDTD calculation. The unit cell used in calculation is a rectangle, consisting of one hole in the center and four quarter-holes at the four corners. The normalized *z*-component *E*-field (E_z) at (B) the *y*-*z* plane for *P*-polarization light and (C) at the *x*-*z* plane for *S*-polarization light. They were calculated at the peak wavelength of λ_{max}^{P} = 925 nm for (B) and λ_{max}^{S} = 1011 nm for (C) as illustrated in Figure 1. The details of FDTD calculations can be found in the experimental section.

Section SVI. Characterization of EENAs

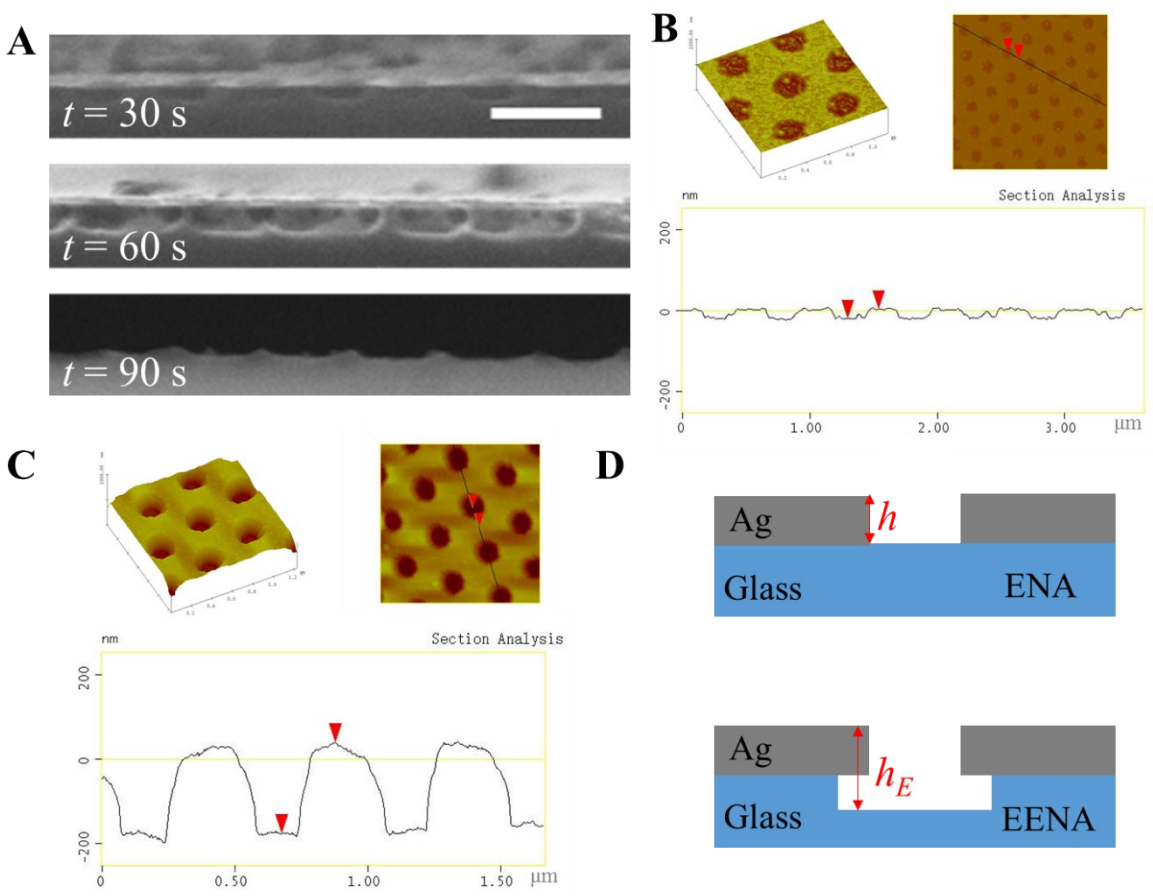

Figure S12. (A) Cross-sectional SEM images of the nanohole array at θ = 0° etched in 1 % HF for t = 30 s, 60 s, and 90 s, respectively. The scale bar represents 500 nm. The film detaches from the substrate when t = 90 s. AFM profiles of (B) the as-deposited nanohole array and (C) the elevated nanohole array etched for t = 60 s at θ = 0°. (D) Schematics of the definition of the height h and h_E for (B) and for (C), which are ~ 23 and ~ 200 nm, respectively.

Section SVII. Sensing Performances of EENAs

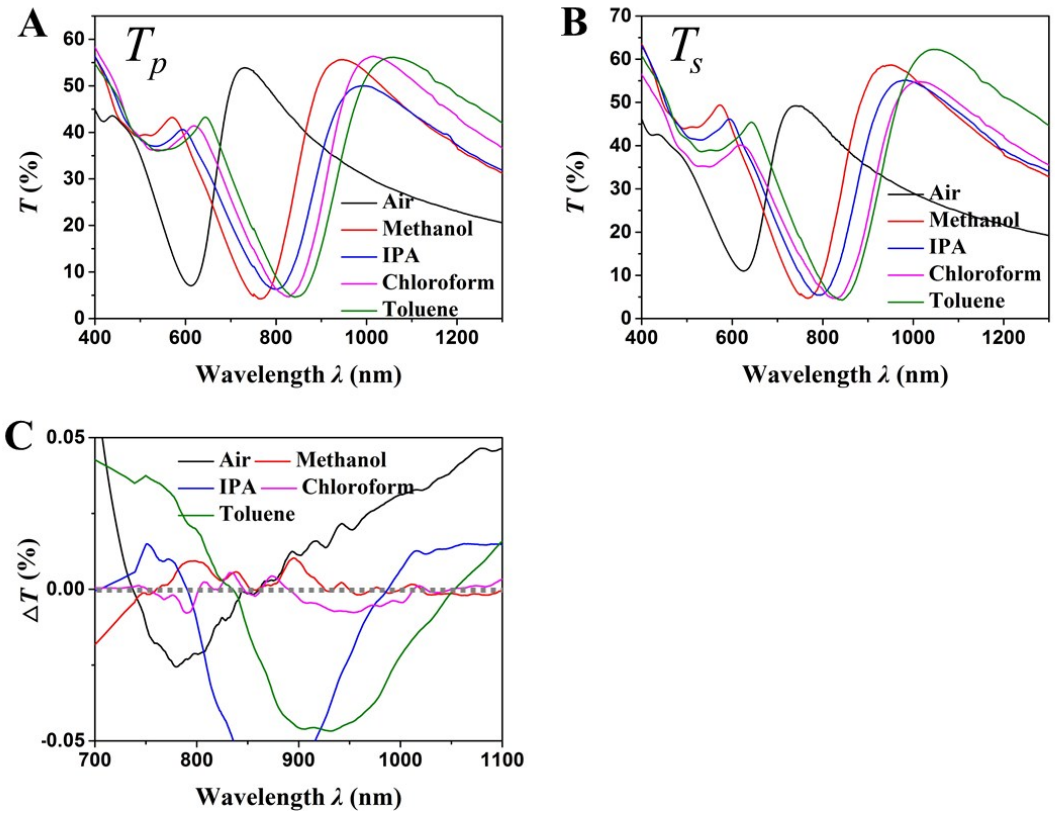

Figure S13. (A) T_p and (B) T_s of the Sample EE$^{15°}$ in different surrounding environments. (C) The corresponding spectra ΔT of the Sample EE$^{15°}$. The grey dotted line indicates $\Delta T = 0$. λ_2 shifts randomly with n due to the small difference in T_p and T_s.

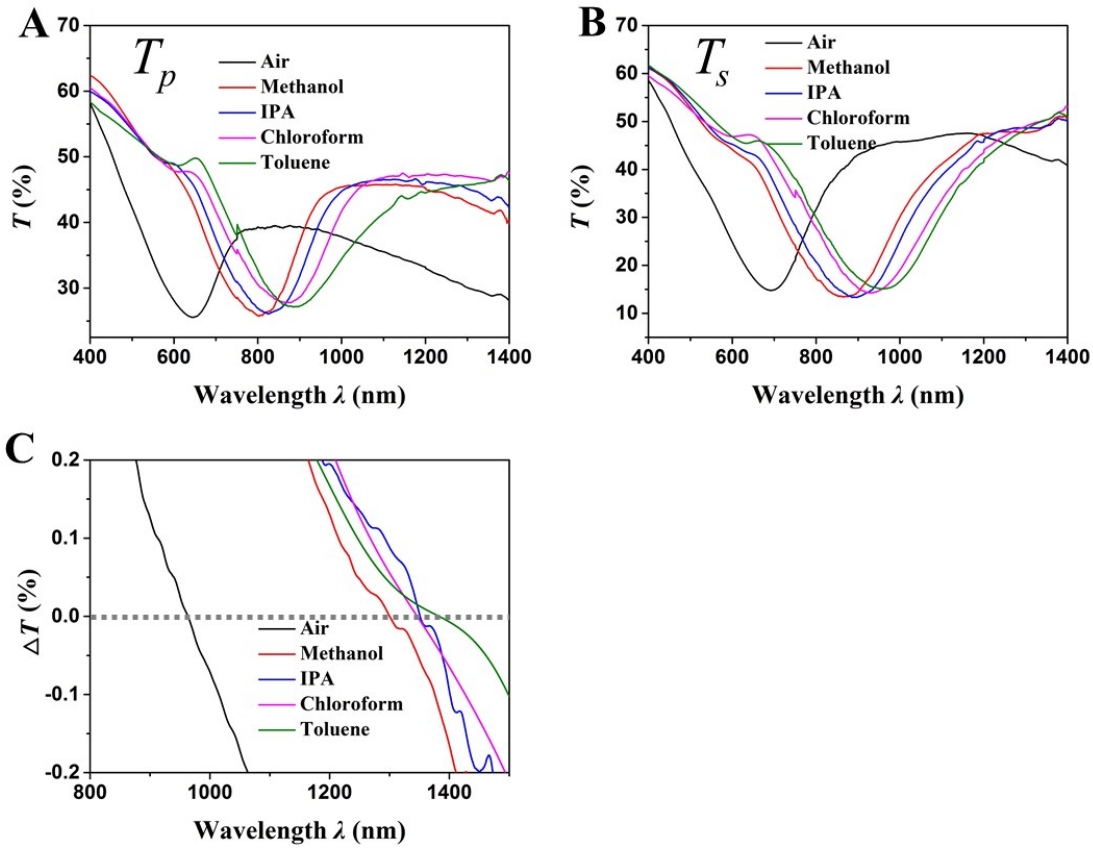

Figure S14. (A) T_p and (B) T_s of the Sample EE$^{45°}$ in different surrounding environments. The peaks are very broad (FWHM > 500 nm). (C) The corresponding spectra ΔT of the Sample EE$^{45°}$. The grey dotted line indicates $\Delta T = 0$. λ_2 shifts unpredictably with n due to the broad peaks.

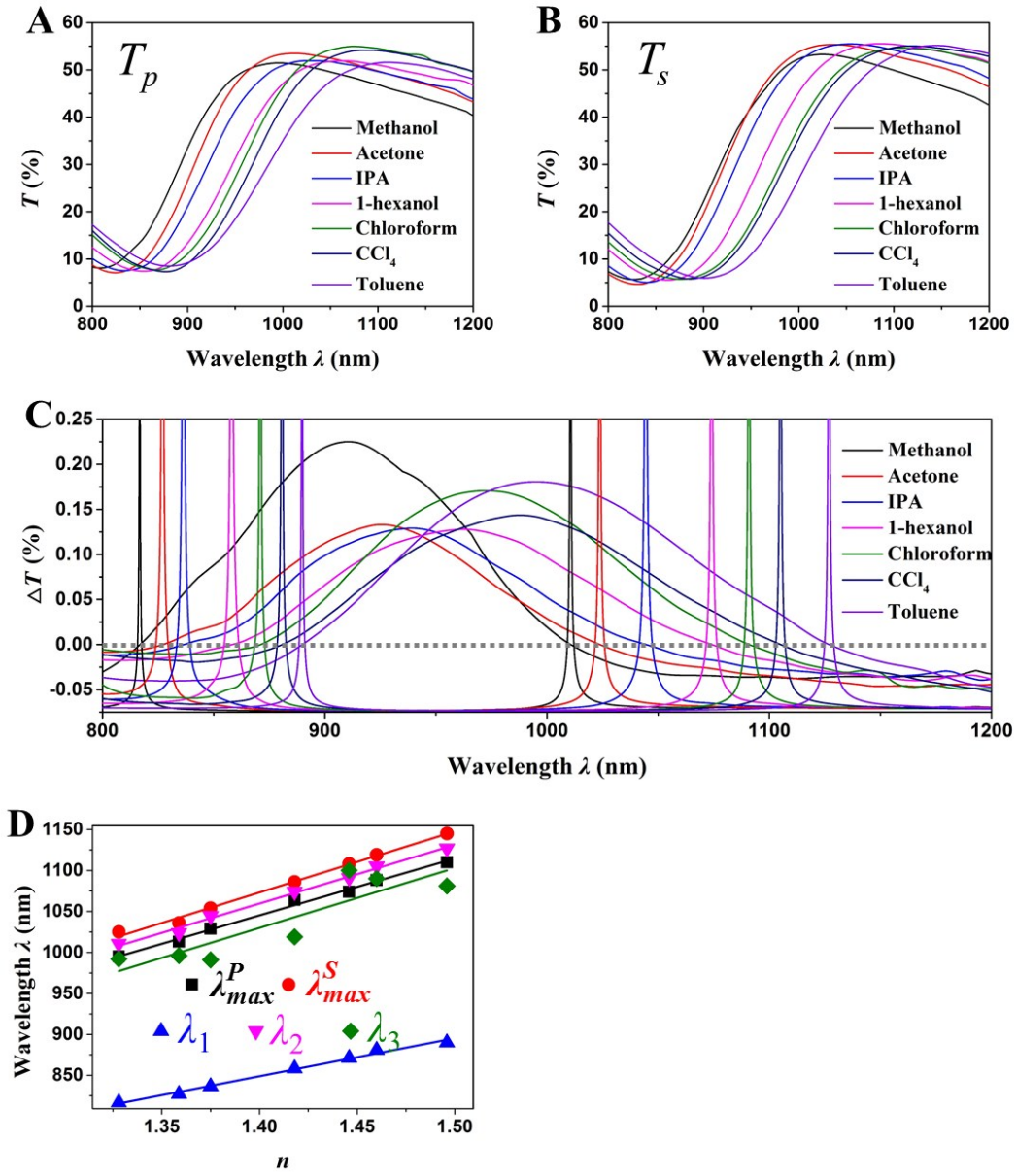

Figure S15. (A) T_p and (B) T_s of the Sample EE$^{30°}$ in different surrounding environments. (C) The corresponding spectra of ΔT and $|\Delta T|^{-1}$ at λ_1 and λ_2. (D) Linear fits of the peak shift of λ^P_{max}, λ^S_{max}, λ_1, λ_2, and λ_3 as a function of n. The fitting linearity of λ_3 (R^2 = 0.74143) is much worse than that of λ_2 (R^2 = 0.99263). This is consistent with the discussion in Section SI.

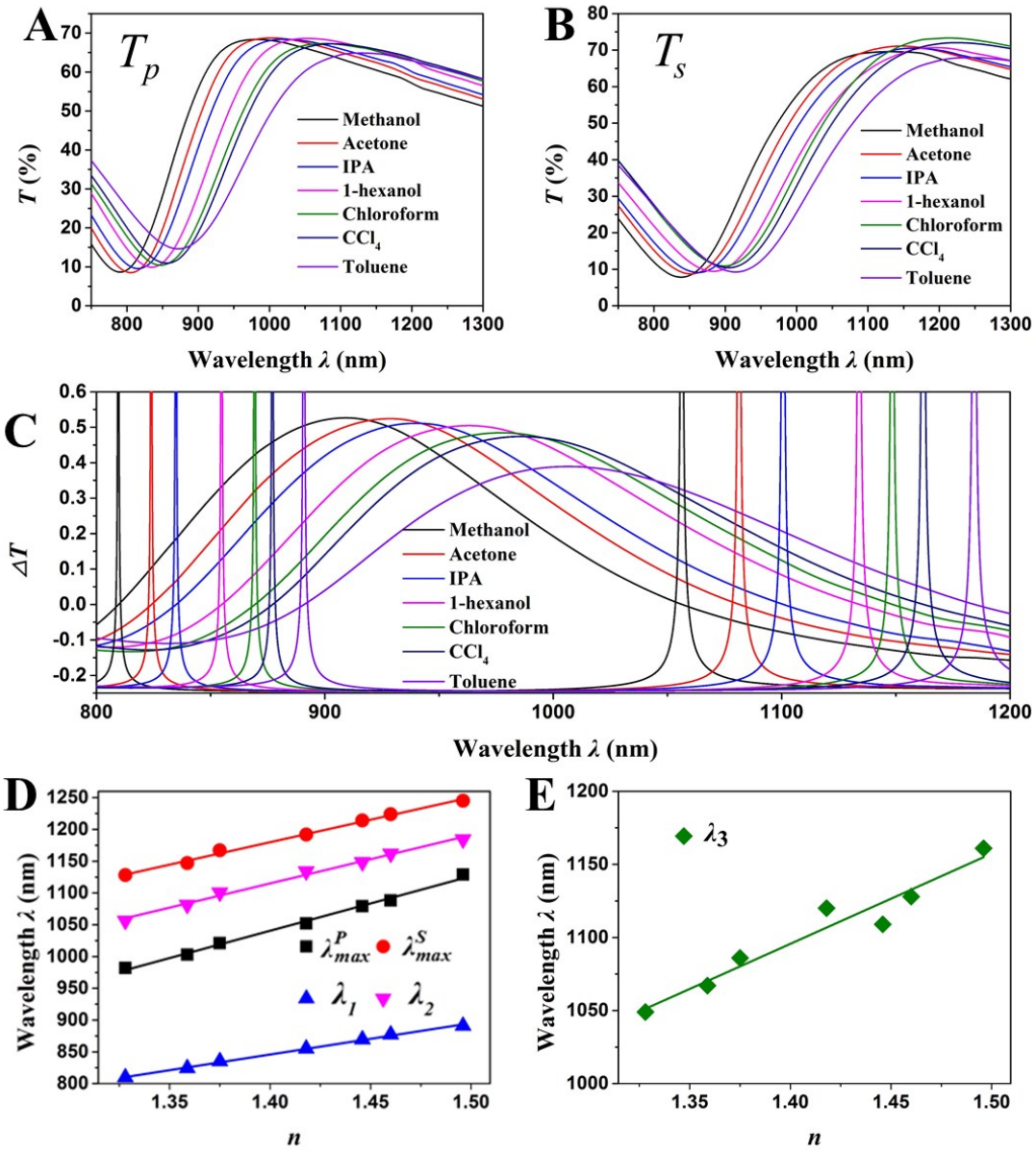

Figure S16. (A) T_p and (B) T_s of the Sample EE$^{40°}$ in different surrounding environments. (C) Spectra of ΔT and $|\Delta T|^{-1}$ at λ_1, and λ_2 in different liquids. (D) Linear fits the peak shift of λ^P_{max}, λ^S_{max}, λ_1 and λ_2 as a function of n. (E) Linear fit of the peak shift of λ_3 as a function of n. The fitting linearity of λ_3 (R^2 = 0.93091) is much worse than that of λ_2 (R^2 = 0.99171). This is consistent with the discussion in Section SI.

Section SVIII. Sensing Performances of Ni Based EENAs

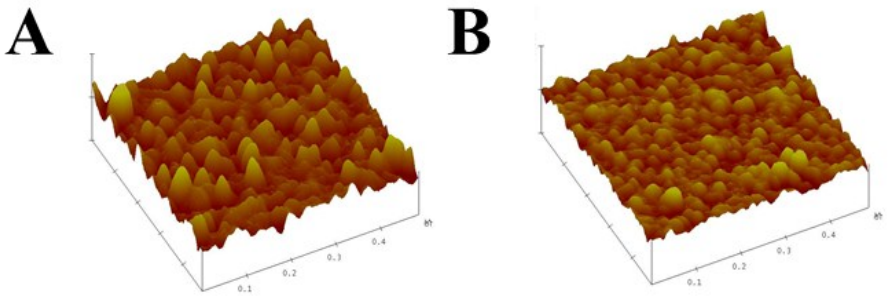

Figure S17. 3D AFM images of the Ag surface on a (A) Ti and (B) Ni adhesive layer.

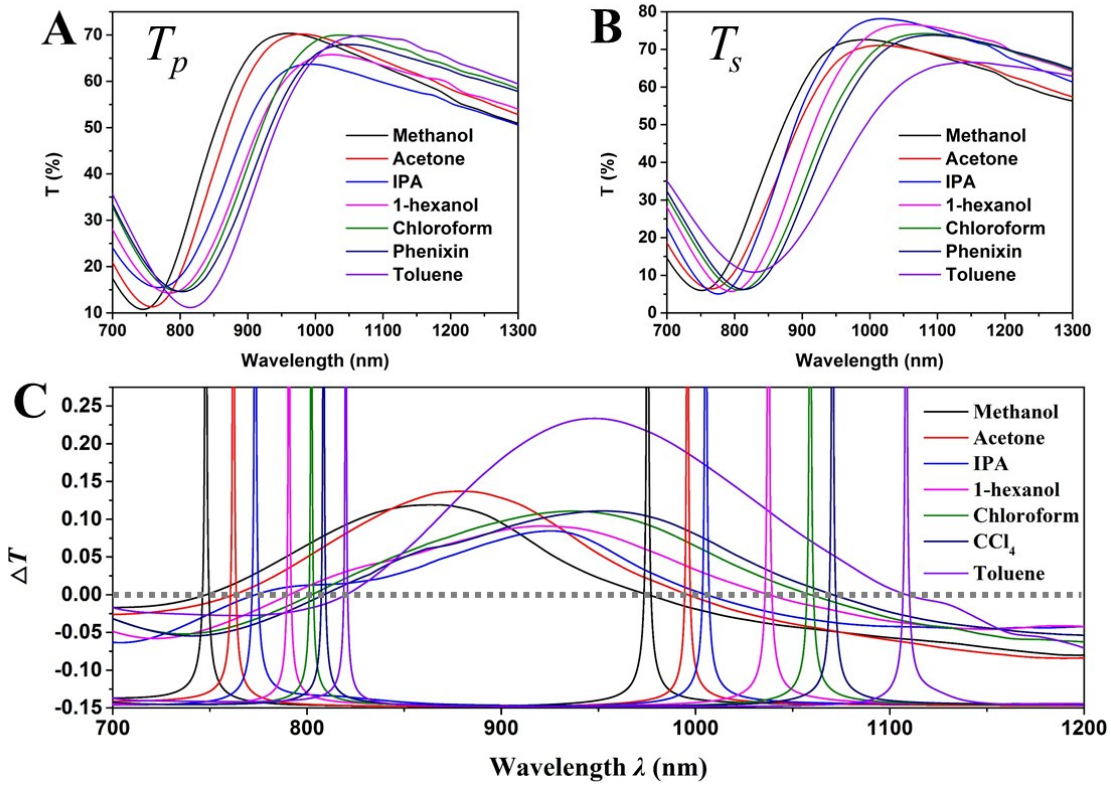

Figure S18. (A) T_p and (B) T_s of the Ni based Sample EE$^{40°}$ in different surrounding environments. (C) The corresponding spectra of ΔT and $|\Delta T|^{-1}$ at λ_1 and λ_2.

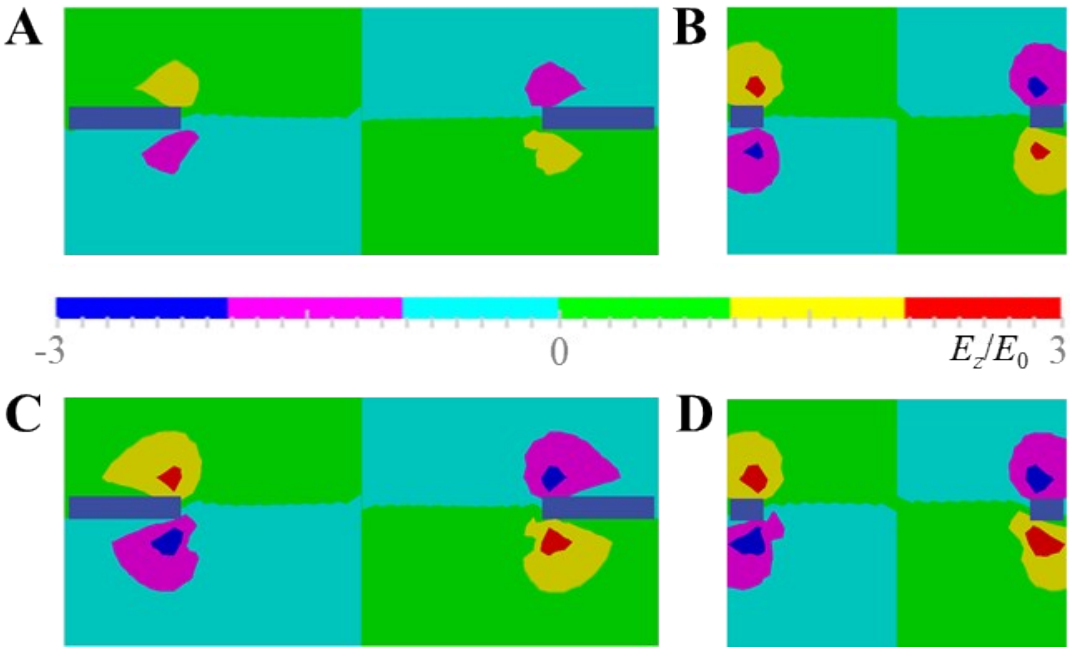

Figure S19. The calculated distribution of *z*-component *E*-field (E_z) of the Sample EE$^{40°}$ on a Ti adhesive layer for (A) *P*- (*y*-*z* plane) and (B) *S*-polarization (*x*-*z* plane). The calculated distribution of *z*-component *E*-field (E_z) of the Sample EE$^{40°}$ on a Ni adhesive layer for (C) *P*- (*y*-*z* plane) and (D) *S*-polarization (*x*-*z* plane). Distributions were calculated at the peak wavelength of λ_{max}^{P} = 788 nm for (A) and (C) and λ_{max}^{S} = 944 nm for (B) and (D).

Section SIX. Absorption of MBA.

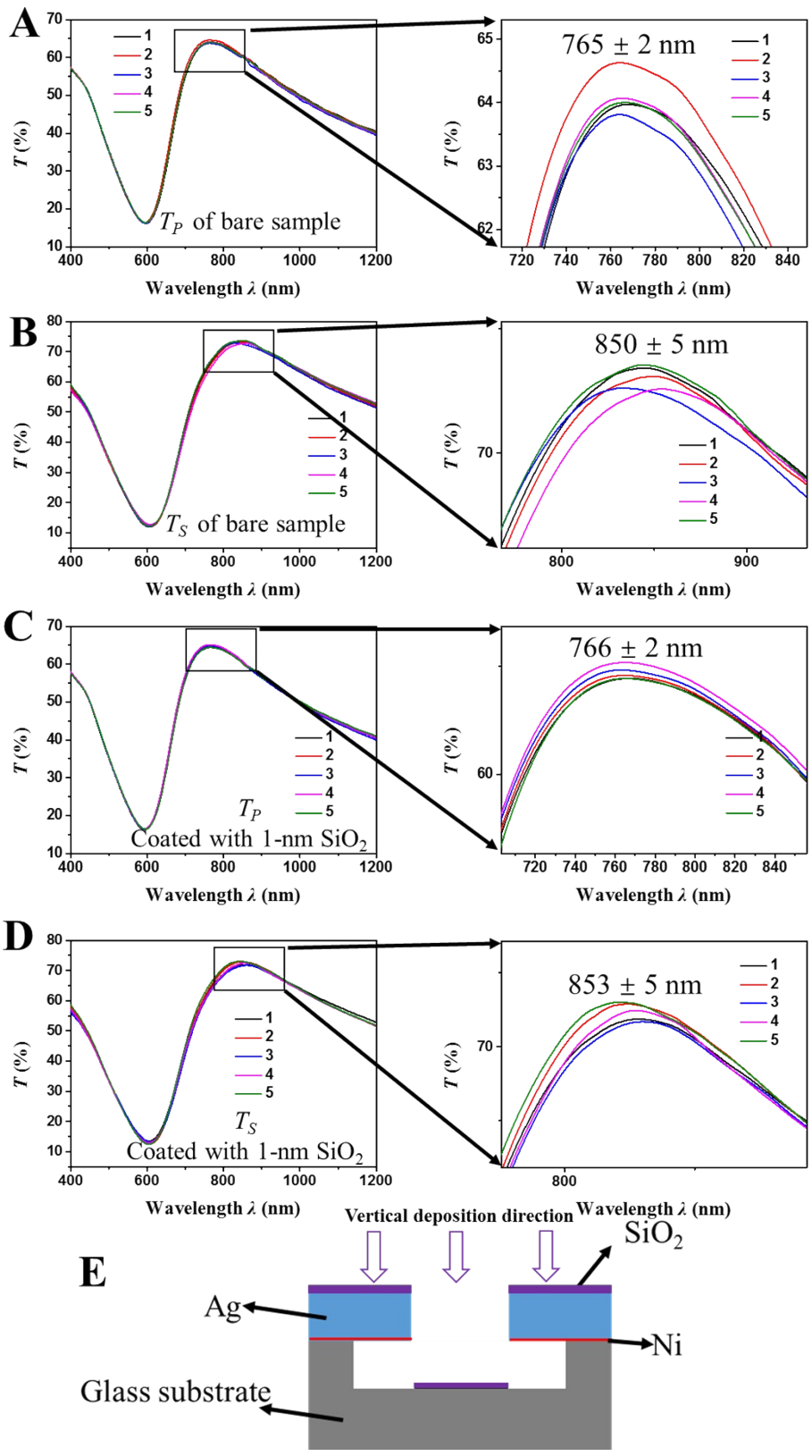

Figure S20. (A) T_P and (B) T_S of the bare $EE^{40°}_{Ni}$ sample. (C) T_P and (D) T_S of the $EE^{40°}_{Ni}$ sample

coated with 1-nm SiO_2 dielectric layer. The test location was marked. The measurements were repeated for five times, which were indicated by the legend in each image. The right figures are the magnification of the peak shift. (E) A schematic showing the structure of the sample coated with 1-nm SiO_2 layer in the experiment. SiO_2 was vertically deposited onto the sample

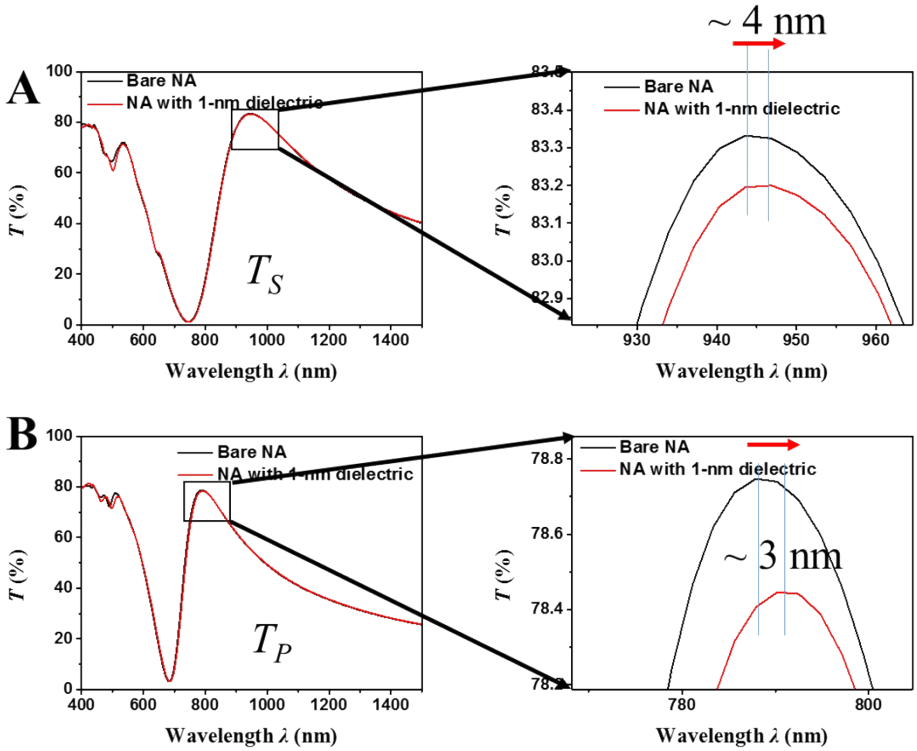

Figure S21. (A) T_S and (B) T_P of the bare $EE^{40^\circ}_{Ni}$ sample and the sample coated with a 1-nm SiO_2 layer. The right figures are the magnification of the peak shift.

Section SX. Detection of RNA Hybridization

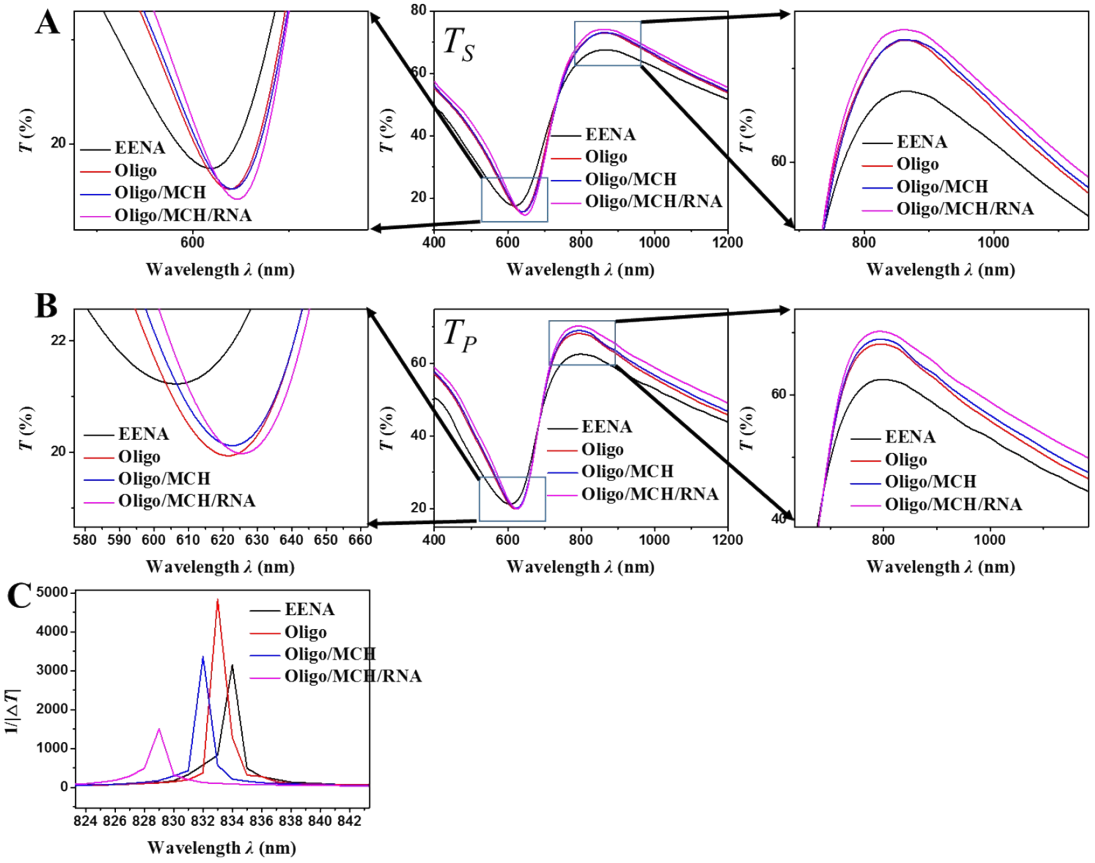

Figure S22. (A) T_S and (B) T_P of the pristine $EE^{40°}_{Ni}$ sample as well as the substrate with Oligo, Oligo/MCH, and Oligo/MCH/RNA. The left and right figures are the magnification of the dip and peak shift, respectively. (C) The spectra $|\Delta T|^{-1}$ of λ_1 of the pristine $EE^{40°}_{Ni}$ sample as well as the substrate with Oligo, Oligo/MCH, and Oligo/MCH/RNA.

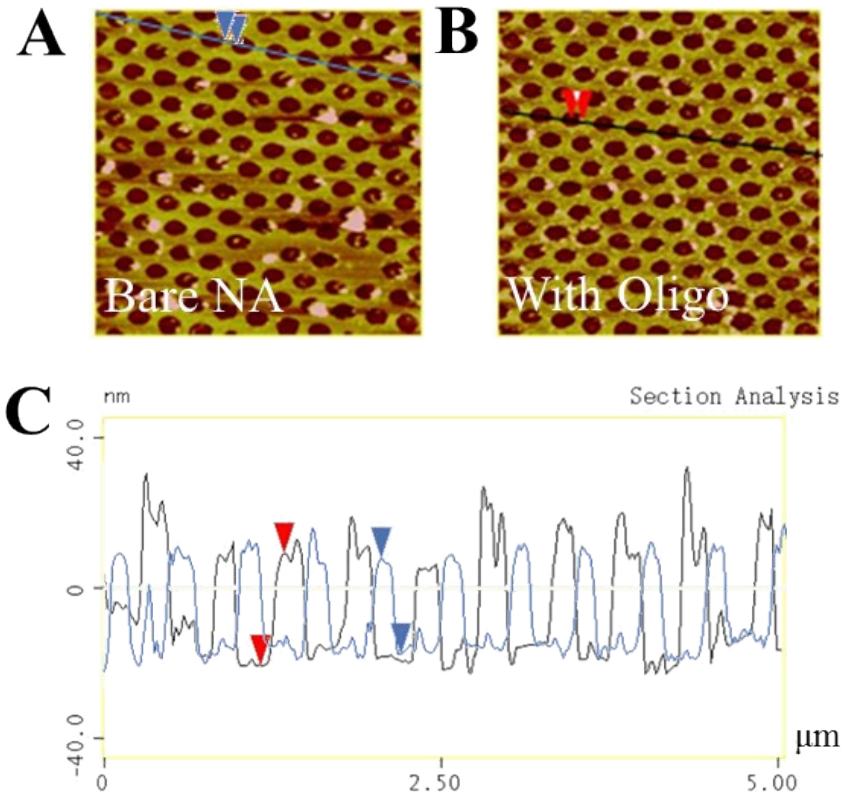

Figure S23. AFM images of the (A) bare $E_{Ni}^{40^\circ}$ sample and (B) Oligo treated $E_{Ni}^{40^\circ}$ sample. (C) Section analysis of the bare $E_{Ni}^{40^\circ}$ sample (blue curve) and Oligo treated $E_{Ni}^{40^\circ}$ sample (black curve). The section is along the blue and black line in (A) and (B), respectively. The thickness of the bare $E_{Ni}^{40^\circ}$ sample and Oligo treated $E_{Ni}^{40^\circ}$ sample is ~ 26 nm and 30 nm, respectively.

Section SXI. Effect of Thickness on Sensing Performances

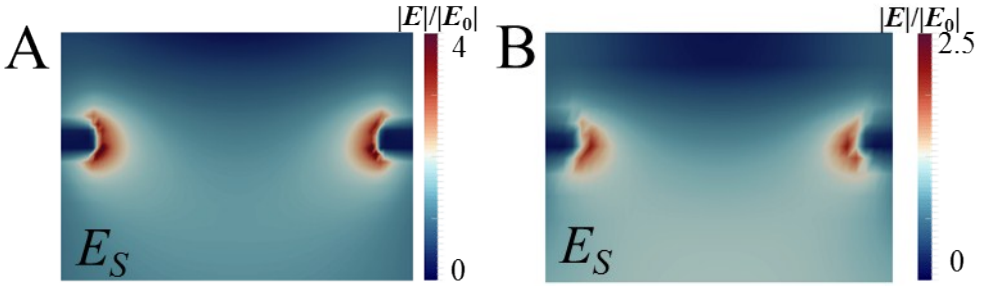

Figure S24. The calculated distribution of the *E*-fields $|E|/|E_0|$ of the Sample $EE_{Ni}^{40°}$ for *S*-polarization (*x*-*z* plane) with the grid size of (A) 4 nm and (B) 8 nm. They were calculated at the peak wavelength of λ_{max}^{S} = 944 nm.

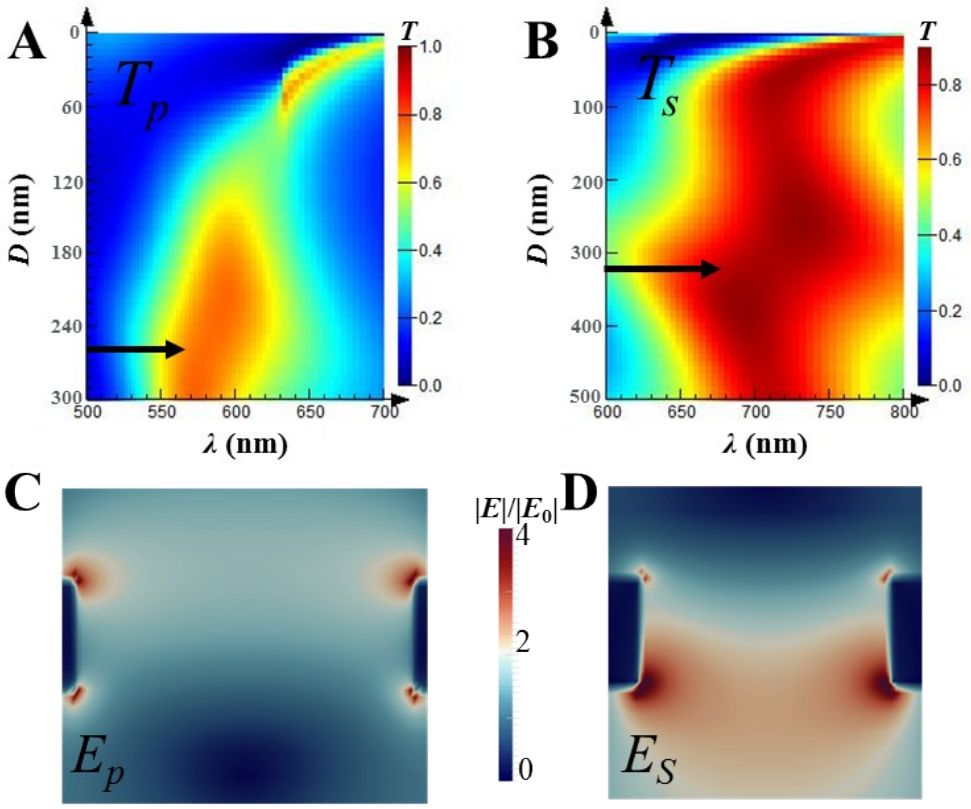

Figure S25. Color map of spectra (A) T_p and (B) T_s of the Ni based Sample EE$^{40°}$ with 100-nm Ag thickness as a function of D. The black arrows point to the inflection point (l_d). The calculated distribution of the E-fields $|E|/|E_0|$ of the Sample $\mathrm{EE}_{\mathrm{Ni}}^{40°}$ with 100-nm Ag thickness for (C) P- (y-z plane) and (D) S-polarization (x-z plane). They were calculated at the peak wavelength of λ_{max}^{P} = 594 nm for (C) and λ_{max}^{S} = 722 nm for (D).

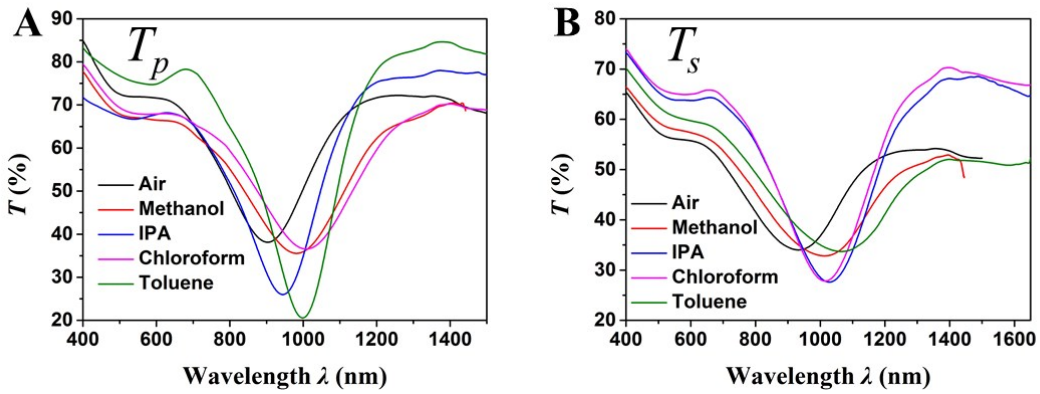

Figure S26. Spectra (A) T_p and (B) T_s of the Sample $E^{30°}$ in different surrounding environments. The Ag thickness is 12 nm. The peaks are too broad to be normalized.

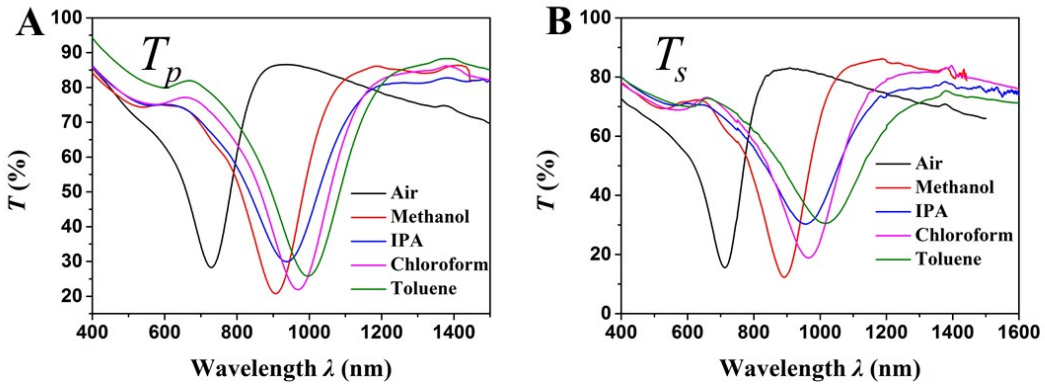

Figure S27. Spectra (A) T_p and (B) T_s of the Sample EE$^{30°}$ in different surrounding environments. The Ag thickness is 12 nm. The peaks are too broad to be normalized.

Reference

1. G. K. Larsen, Y. He, W. Ingram, Y. Zhao, *Nano Lett.* **2013**, *13*, 6228.